Tight Junction-high and CDH17-positive cell population is the Source of Colorectal Cancer Liver Metastases

Lluís Espinosa

lespinosa@imim.es

Institute Hospital del Mar d'investigations Mediques-IMIM https://orcid.org/0000-0002-2897-4099

Daniel Alvarez Villanueva

Institute Hospital del Mar d'investigations Mediques-IMIM

Maria Maqueda

Hospital del Mar Research Institute

eric canton

Institute Hospital del Mar d'investigations Mediques-IMIM

Evelyn Andrades

Hospital del Mar Research Institute (HMRIB)

Joan Bertran

Universitat de Vic - Universitat Central de Catalunya

Monica Larrubia

Hospital del Mar

Anna Tramuns

Hospital del Mar

Violeta garcia-hernandez

Hospital del Mar Research Institute

Teresa Lobo-Jarne

Hospital 12 De Octubre Research Institute (i+12) https://orcid.org/0000-0002-1632-438X

josune alonso

Hospital del Mar Research Institute

dina harti

Hospital del Mar Research Institute

Kieran Wynne

University College Dublin

indrani bera

University College Dublin

David Matallanas

University College Dublin https://orcid.org/0000-0002-2360-3141
Patricia Herrero
Hospital del Mar Research Institute
Maria Martínez-Iniesta
Catalan Institute of Oncology (ICO) https://orcid.org/0000-0001-6252-6671
Alberto Villanueva
Institut Català d'Oncologia (ICO)-Institut d'Investigació Biomèdica de Bellvitge (IDIBELL)
https://orcid.org/0000-0001-5164-0006
Anna Bigas
Hospital del Mar Research Institute
Mar Iglesias
Hospital del Mar

Article

Keywords:

Posted Date: July 9th, 2025

DOI: https://doi.org/10.21203/rs.3.rs-6998644/v1

Additional Declarations: There is **NO** Competing Interest.

Abstract

The IKKα kinase is increasingly emerging as a critical regulator of oncogenic and therapy-resistance elements including ATM/DDR, BRD4, and JAK/STAT, operating independently of canonical NF-κB signaling. Here, we reveal an unexpected metastasis suppressor role for IKKα in colorectal cancer (CRC). Specifically, genetic or pharmacological inhibition of IKKα in patient-derived organoids (PDOs) drives the emergence of tightly clustered cell populations, mediated by the stabilization of tight junction components ZO-1 and CLDN2, which display a markedly increased metastatic potential in vivo. Single-cell RNA sequencing of CRC PDOs uncovered three epithelial subpopulations (C2, C4, C8), enriched in tight junction and metastasis-associated EpiHR gene signatures. Strikingly, only C8 markers, particularly CDH17, were consistently enriched in liver metastases derived from primary PDOs. Immunohistochemistry confirmed that metastatic lesions were predominantly composed of CDH17^{+} cells. Disruption of CLDN2, either genetically or pharmacologically, completely abrogated the metastatic advantage conferred by IKKα loss.

Together, our findings identify a CDH17^{+}/CLDN2^{+} epithelial subpopulation as the source and metastatic driver in IKKα-deficient CRC. These results reveal a previously unrecognized link between tight junction remodeling and metastatic dissemination, offering a novel and targetable vulnerability in aggressive colorectal tumors.

BACKGROUND

Colorectal cancer (CRC) remains the second leading cause of cancer death worldwide. Although primary CRC tumors are generally completely eradicated after surgery, up to 50% of patients, a proportion that varies greatly depending on the stage of the tumor at the time of diagnosis, suffer tumor metastases and eventually die (reviewed in [1]). Epithelial-to-mesenchymal transition (EMT) has been classically linked to the capacity of cancer cells to detach from epithelial layers to initiate metastasis (reviewed in [2–4]). Different structures such as adherens and tight junctions are essential for the maintenance of epithelial identity and tissue integrity and, in fact, one of the main promoter of EMT is the loss of the adherens protein E-Cadherin during tumor invasion [5] imposed by the transcriptional repressor SNA1 [6,7]. However, a hybrid EMT phenotype of epithelial cancer cells was found to provide superior metastatic activity compared to a pure epithelial or mesenchymal phenotype [8–10].

There is substantial evidence indicating that cancer cell migration in clusters (collective migration), which is regulated by various mechanisms including hypoxia [11] and the composition of cell-cell junctions [12], favors the survival of circulating cells, resulting in increased metastatic activity in several cancer models [11,13–16]. Cellular clusters have been found to be either homogenous, composed only by epithelial tumor cells, or heterogeneous containing epithelial tumor cells and non-tumor cells such as white blood cells, which provide further oncogenic properties to cancer cells (reviewed in [17]. Tight junction proteins, including TJP1/ZO-1 (henceforward ZO-1) play a critical role in the establishment of cell-cell interactions

and the maintenance of stable epithelial structures through the anchoring and clustering of transmembrane adhesion molecules with the cellular cytoskeleton [18].

Inflammation and innate immunity, linked to NF-κB signaling, has been repeatedly implicated in cancer initiation and progression in multiple systems [19–21]. Activation of NF-κB signaling is primarily dependent on a cytosolic kinase complex formed by IKKα, IKKβ and NEMO subunits. In addition, nuclear IKK, which is induced by oncogenes such as mutant BRAF and KRAS or by DNA-damaging agents, exerts additional pro-tumorigenic roles such as apoptosis inhibition [22–25], promotion of DNA damage repair through ATM phosphorylation [26] or activation of BRD4 and JAK/STAT3 pathways in cancer [27]. Nuclear active IKKα is also associated with metastasis promotion in prostate cancer [28] and squamous cell carcinoma [29] by transcriptional repression of the tumor and metastasis suppressor *Maspin* [30]. IKK signaling was found to regulate the expression of the stemness- and metastasis-related receptor CD44 [31,32].

Here, we demonstrate that the functional inactivation of IKKα induces the stabilization of tight junction elements, resulting in cellular clustering and increased metastatic activity *in vivo*. We identified three distinct epithelial clusters characterized by high expression of tight junction and EpiHR signatures. Cluster 8, identifiable by CDH17 expression, is significantly more prominent in IKKα KO cells and comprises the majority of tumor cells in PDO-derived metastases.

RESULTS

Abrogation of the IKKα kinase activity promotes liver metastasis in CRC patient-derived organoids

Several lines of evidence indicate that IKKα exerts pro-tumorigenic activities in human cancer, but its role in metastasis has not been clearly established. To test its role in CRC metastatic capacity, we generated two different IKKα KO PDO lines. We experimentally tested the metastatic capacity of WT and IKKα KO PDO5 cells upon intrasplenic transplantation in nude mice. Unexpectedly, IKKα-depleted PDO5 cells showed significantly higher metastatic activity than WT PDO cells, both in number and size of metastases, and comparable to that observed in mice treated with vemurafenib, which inhibits BRAF-dependent IKKα activity in cancer cells [25,33,34] (Figs. 1A and 1B). By histopathological examination and IHC analysis, we found that liver metastases derived from IKKα KO PDO5 cells were organized as compact glandular structures, much larger and more proliferative, based on the proliferation marker KI67, than the corresponding IKKα WT metastases. No activated SMA1-positive fibroblasts were found within the large IKKα KO glands (Fig. 1C). Increased metastatic activity was observed using an independent patient-derived IKKα KO PDO line (Figure S1).

These results demonstrate that IKKα may act as a metastasis suppressor in human CRC.

Functional depletion of IKKα alters the migratory behavior of cancer cells

We investigated whether the higher metastatic activity observed in IKKα KO cells was due to an increased cell motility. Using DLD1 and CaCo2 CRC cells and wound-healing assays as experimental model, we found that cell migration was significantly reduced upon IKKα KO (Fig. 2A and S2A), similar to DLD1 and HCT116 cells treated with the BRAF/IKKα inhibitor AZ628 (Figures S2B and S2C). We found no difference between untreated and AZ628-treated IKKα KO cells (Fig. 2A and S2A), further indicating that the effect of AZ628 on cell migration was related to its inhibitory activity on IKKα.

We then took advantage of the fact that PDO cells, which form spheres in 3D Matrigel cultures, produce flat colonies that adhere and spread across plastic plates when adapted to 2D conditions (Fig. 2B). Depletion of IKKα virtually abolished the ability of PDO cells to adhere and spread on plastic plates, keeping them as spherical structures (Fig. 2C and S2D). The same adhesion and migration impairment was observed upon AZ628 treatment of PDO cells (Figure S2E). We further tested the effects of IKKα depletion or inhibition in transwell cell migration assay. Treatment of HCT116 and DLD1 cells with AZ628 significantly reduced their capacity to migrate across the transwell filters (Fig. 2D and S2F). Interestingly, the majority of AZ628-treated cells that migrated through the membrane were distributed in clusters compared to control cells that migrated as single cells (Fig. 2D, 2E, S2F and S2G). Increased cellular clustering was also detected by seeding single IKKα KO CaCo2 cells under non-adherent conditions (Figure S2H).

These results indicate that abrogation of IKKα function reduces the migratory capacity of CRC cells while promoting cellular clustering.

IKKα shapes tight junction architecture via ZO-1 and CLDN2 regulation

We hypothesize that IKKα may affect cellular clustering by directly regulating cell-cell contact elements. By examining phospho-proteomic data previously generated by our group [26] (raw data available at PRIDE: PXD008932), we identified the tight junction protein ZO-1, mostly at serine 617, as a potential phosphorylation target of IKKα (Figure S3A). By IHC and IF analysis, we detected a significant increase of ZO-1 positivity at the cell-cell contacts in IKKα KO PDO cells, both *in vitro* (Figure S3B) and the PDO5-derived liver metastases (Fig. 3A), and aberrant ZO-1 localization at the edge of the colonies in IKKα KO CaCo2 cells (Fig. 3B). Altered ZO-1 distribution was also observed upon AZ628 treatment of CaCo2, HT-29 M6 and HCT116 cells (Figure S3C-E). The efficiency of IKKα inhibition by AZ628 was confirmed by Western Blot (WB) analysis using the antibody against p-IKKα/β (Figure S3F). Further indicating that IKKα-dependent phosphorylation of ZO-1 affects its subcellular distribution, the ZO-1 S617A phosphorylation-deficient mutant shows a marked shift from its localization in cell-cell contacts to the

membranes bounding the Caco2 colonies (Figure S3G). This pattern closely mirrors that seen in IKKα KO cells, where phosphorylation at S617 does not occur.

We then tested whether altered ZO-1 distribution was associated with changes in ZO-1 protein levels. WB analysis of WT and IKKα KO cells demonstrated that IKKα depletion led to an increase in the amount of ZO-1 protein in the different cellular systems tested (Fig. 3C), which was not due to an increase in RNA levels (Figure S3H). Treatment of CaCo2 cells with the protein synthesis inhibitor cycloheximide (CHX) followed by WB analysis revealed an increased half-life of the ZO-1 protein in IKKα KO cells (Fig. 3D), suggesting that IKKα-dependent phosphorylation may favor ZO-1 destabilization. In support of this concept, we found that both IKKα (Fig. 3E) and active p-IKK (Fig. 3F), which are mostly distributed throughout the cell cytoplasm, specifically colocalized with residual ZO-1 protein on cell membranes at the periphery of colonies in IKKα WT CaCo2 cells. Some p-IKK staining, likely corresponding to active IKKβ, still colocalized with ZO-1 in the membrane of IKKα KO CaCo2 cells (Fig. 3F). These results suggest that IKKα-dependent phosphorylation destabilizes ZO-1 and suppresses the formation of aberrant, mislocalized tight junction-like structures.

We performed IHC analysis of several cell-cell contact elements in the liver metastases derived from WT and IKKα KO PDO5 cells. We detected increased amounts of CLDN2, a key structural and functional component of the tight junctions, in IKKα KO-derived tumors (Fig. 3G). We did not detect CLDN2 as a candidate phosphorylation substrate of IKKα in the phospho-proteomics data. However, bulk RNA-seq analysis of PDO5 revealed a significant increase in CLDN2 mRNA levels in IKKα KO cells (Fig. 3H and Supplementary Table S1), which was confirmed by qPCR (Fig. 3I), WB (Fig. 3J) and IF/IHC analysis (Fig. 3K, 3L) of several IKKα KO CRC models.

Together these results indicate that IKKα directly regulates tight junction integrity by modulating the levels and distribution of key cell-cell contact proteins, both *in vitro* and *in vivo*.

Tight junction and Epi-HR signature-enriched cell populations drive liver metastasis and predict poor prognosis

To further investigate whether tight junction stabilization might underlie the increased metastatic activity observed in IKKα KO cells, we performed scRNA-seq analysis of WT, IKKα KO, and IKKα KO PDO5 cells treated with YM201636, which disrupts CLDN2 recycling and function [35]. From this analysis, we defined 10 distinct epithelial (EPCAM+) cell clusters (Fig. 4A) that are represented in our three experimental models (Fig. 4B). Per cell, we scored the tight junction signature from the Gene Ontology database (GO:0120193 term) and the epithelial high-relapse (EpiHR) signature obtained from a mouse model of metastatic CRC [36]. We found that both the EpiHR and tight junction signatures were enriched in clusters 2 (C2), 4 (C4), and 8 (C8) (Fig. 4C), with more than 50% of all cells in these clusters classified as EpiHR-high (Fig. 4D). Unexpectedly, the stem cell marker LGR5 and the proliferation marker KI67 were primarily absent from these particular clusters (Figure S4A), suggesting that highly proliferative stem cells may not play a major role in tumor metastasis. The top 50 marker genes in C2, C4 and C8 minimally

overlapped with the EpiHR signature (Fig. 4E, Supplementary Table S2). Moreover, survival analysis conducted over in-house CRC metacohort, with 843 Stage II and III patients, demonstrated the adverse prognostic value of those C2, C4 and C8 marker genes (Figure S4B). Further analysis of scRNA-seq data revealed the significant upregulation of C2 and C8 gene signatures in IKKα KO cells (Figure S4C). Upregulation of these clusters at the transcriptional levels was further supported by proteomic data (Supplementary Table S3). Additionally, C8 signature was significantly enriched in PD05-derived liver metastases compared to primary PDO cells in bulk RNA-seq data from both the WT and IKKα KO models (Supplementary Tables S4); Figs. 4F). This significant enrichment was not observed for the rest of cluster signatures (Figure S4D). Notably, treatment with YM201636 partially reversed the upregulation of most metastasis-associated C8 signature genes (Figure S4C) and reduced the proportion of C8 cluster cells (from 8.3–3.9%, Fig. 4B). Overall, these results may indicate/suggest a functional role of this cluster in the metastatic behavior of PDO

To further investigate whether the C8 subpopulation was responsible for the higher metastatic activity of IKKα KO cells, we selected membrane markers specifically enriched in clusters C2, C4, and C8, which are candidates for the source of metastases. Based on our scRNA-seq data, we selected SLC14A1 for C2, IL6R for C4, and CDH17 for C8 (Figure S4E). Flow cytometry analysis revealed a variable proportion of these cell populations among the total PDO5 cells (Figure S4F), a proportion that increased in IKKα KO cells, as determined by immunohistochemistry (IHC) (Fig. 4G). Increased expression of SLC14A1 (C2) and CDH17 (C8) markers was shown in IKKα KO cells by scRNA-seq data (Figure S4E). Interestingly, CDH17 was massively upregulated in the vast majority of both wild-type (WT) and IKKα KO PDO5-derived metastases (Fig. 4G), supporting the notion of clonal selection and pointing to the C8 cell cluster as the most likely source of metastasis.

Together, our results indicate high overlap between tumor cell populations with high tight junction activity and those characterized by the metastasis-associated EpiHR signature [36]. However, a subset of these cells, defined by expression of the membrane marker CDH17, is responsible for the high metastatic activity of IKKα KO colorectal cancer PDOs.

CLDN2 as a therapeutic target to counteract IKK deficiency–driven metastasis

One member of the CLDN family, CLDN18.2, is expressed in a variety of cancers, including gastric and pancreatic tumors, and blocking antibodies against this protein have shown efficacy in the treatment of metastatic gastric cancer [37,38]. We investigated whether interfering with CLDN2, which reduces the expression of C8 metastatic cluster signature (Figure S4C), may reverse the migratory phenotype imposed by IKKα depletion in CRC cells. We first performed wound healing assays in IKKα KO CaCo2 and HT-29 M6 cells untreated or treated with YM201636. YM201636 treatment was sufficient to restore the migratory activity of IKKα KO cells in wound healing assays to the level of WT cells, both after chronic exposure or after 16h treatment followed by drug washout (Fig. 5A and 5B). Similarly, YM201636

treatment reverted the adhesive/migratory properties of IKKα KO PDO5 cells adapted to grow in 2D cultures (Fig. 5C and 5D). To confirm that the observed effects were specifically due to CLDN2 inhibition, we knocked down CLDN2 in CaCo2 and PDO5 IKKα KO cells using three independent shRNAs (Figures S5A and S5B). CLDN2 silencing partially restored the cell adhesion defects imposed by IKKα deficiency in PDO5 cells (Fig. 5E) and migratory phenotype in Caco2 cells (Figs. 5F and S5C). To provide proof of concept for the potential use of CLDN2 inhibition in CRC therapy, we performed *in vivo* metastasis assays by intrasplenic implantation of IKKα KO PDO5 cells untreated or treated with YM201636 for 16 hours prior to injection. Pretreatment of IKKα KO cells with YM201636 significantly reduced the number and size of metastases arising in the liver of nude mice without having a significant impact on cell viability prior to injection (Figure S5D). Genetic silencing of CLDN2 in IKKα KO PDO5 cells with three distinct shRNAs consistently mirrored the suppression of metastatic potential observed upon YM201636 treatment (Figs. 5G-L).

Our findings reveal a distinct cell cluster enriched in tight junction components and CLDN17 as a source of liver metastasis. Additionally, we demonstrate that CLDN2 plays a key role in mediating the metastasis-suppressor function of IKKα in colorectal cancer. Together these results support the therapeutic potential of targeting tight junction elements as a viable strategy to limit metastatic progression in CRC patients

DISCUSSION

The IKKα kinase, as well as other members of the NF-κB pathway, are generally considered to be drivers of tumorigenesis [39–41] and metastasis [28,29,42], making IKKα inhibitors candidate targets for treatment [34,43–45]. In this work, using several experimental strategies and various IKKα KO CRC models, we have found that IKKα activity is required for the proper establishment of the cell-cell contacts. Thus, IKKα depletion or inhibition led to a general disorganization of the tight and adherens junctions that correlates with a reduced cell migration and a change in the migratory mode of CRC cells from single migration (classical EMT) towards a collective migration. A reduced migratory and invasive capacity *in vitro* has also been observed in prostate cancer cells using general IKK inhibitors [46], which was interpreted as an anti-metastatic effect. Altered distribution of ZO-1 leading to increased collective migration is also observed in colorectal cancer cells expressing high levels of PLP2 [47]. Interestingly, PLP2 is significantly increased in the liver metastases derived from PDO5 cells (Supplementary Table S1) suggesting that altered ZO-1 activity is still required during metastatic colonization. Here, we have experimentally demonstrated that changes in the migratory mode associated with differential tight junction activity have a more pronounced impact on the *in vivo* metastatic activity of cancer cells than the speed at which cancer cells migrate. This concept, supported by work from several groups [14–16,48,49], contrasts with the canonical view of loss of epithelial features and acquisition of mesenchymal features (EMT) as the main pathway for metastasis [3,7,50], which has recently been modulated by incorporating the concept of EMT transition states [51–53].

The evidence that collective cancer cell migration is increasingly achieved may not only require a rethinking of the concept of pure EMT as a metastatic driver, but it may also affect the well-established concept that poorly differentiated tumors with a clear EMT phenotype should by definition be more metastatic. We have here provided robust preclinical evidence that targeting CLDN2 in patient-derived tumor cells with high levels of tight junction proteins, such as those with IKKα deletions, prevents metastasis. These results may stimulate further investigations focused on the possibility of generating compounds against CLDN2, such as mid-affinity antibodies, that selectively target highly metastatic tumor cells without affecting other tissues that express lower levels of CLDN2, such as kidney or liver (observed in available data from https://www.proteinatlas.org). We are also exploring the possibility of using such compounds in combination with therapies involving BRAF inhibitors, which may promote tumor metastasis, likely related to their ability to inactivate IKKα in cancer cells.

In addition to tight junction elements, genes representative of cluster 8, in our scRNAseq, could be incorporated into clinical practice as biomarkers and/or therapeutic targets, after further investigation. Of particular interest are genes previously associated with cancer, metastasis or therapy resistance, such as TFF1 [54–56], TFF3 [57,58].

In conclusion, we have now provided experimental evidence that IKKα, likely modulated by the pro-anti-inflammatory microenvironment at specific tumors, may not only exert pro-tumorigenic activities, but also anti-metastatic functions, by preventing collective migration, which is increasingly recognized as a poor prognostic factor. Moreover, we identified 3 specific cell clusters within the PDO5 population that show a concomitant enrichment of the tight junction and EpiHR signatures, and are characterized by specific transcriptional programs that are selected in liver metastatic outgrowths as determined by bulk RNA-seq analysis. We expect this investigation to have a profound impact on future clinical practice.

CONCLUSIONS

We have now provided experimental evidence that IKKα, likely modulated by the pro-anti-inflammatory microenvironment at specific tumors, may not only exert pro-tumorigenic activities, but also anti-metastatic functions, by preventing collective migration, which is increasingly recognized as a poor prognostic factor. Moreover, we identified 3 specific cell clusters within the PDO population that show a concomitant enrichment of the tight junction and EpiHR signatures. One of this cellular clusters characterized by the expression of the membrane markers CLDH17 is specifically selected in the liver metastatic outgrowths as determined by bulk RNA-seq analysis. Whether IKKα-deficiency promotes the metastatic activity of CRC in patients remains to be investigated.

METHODS

Colorectal Cancer cell lines

CRC cell lines CaCo2, HT-29 M6, HCT116 and DLD1 were obtained from the American Type Culture Collection (ATCC, USA). Cell lines were grown in Dulbecco's modified Eagle's medium (Invitrogen) plus 10% fetal bovine serum (Biological Industries) and were maintained in a 5% CO2 incubator at 37 °C.

PDO and culture conditions

Human colorectal tumors were obtained from Parc de Salut MAR Biobank (MARbiobank. Written informed consent was obtained from all participants and protocols were approved by Hospital del Mar' Ethics Committee (approval number 2019/8595/I), the Spanish regulations, and the Helsinki declaration's Guide. For PDOs generation, primary or xenografted human colorectal tumors were disaggregated in 1.5 mg/mL collagenase II and 20 µg/mL hyaluronidase after 40 min of incubation at 37 °C, filtered in 100 µm cell strainer, and seeded in 50 µL Matrigel in 24-well plates. After polymerization, 450 µL of complete medium was added (DMEM/F12 plus penicillin (100 U/mL) and streptomycin (100 µg/mL), 100 µg/mL Primocin, 1× N2 and B27, 10mM Nicotinamide; 1.25mM N-Acetyl-L-cysteine, 100 ng/mL Noggin and 100 ng/mL R-spondin-1, 10 µM Y-27632, 10nM PGE2, 3µM SB202190, 0.5µMA8301, 50 ng/mL EGF and 10nM Gastrin I). In the different experiments, PDOs were collected and digested with an adequate amount of trypsin to single cells and replated in culture. Cultures were maintained at 37 °C, 5% CO2 and medium changed every week. PDOs were expanded by serial passaging and kept frozen in liquid Nitrogen for being used in subsequent experiments. Mutations identified in the different PDOs were: PDO5; KRAS G12D (66.43%), PDO4; TP53 I254T (100%)/EGFR S464L (97.21%) and PDO8; TP53 Q192stop (98.46%)/KRAS G13C (67.27%).

Animal studies

For metastasis assays, equivalent amounts of disaggregated PDO cells were injected in the spleen of thymic nude mice (strain: Hsd:Athymic Nude-Foxn1nu; 5–7-week-old males). Spleens were surgically removed 24-48 hours after injection. Tumor growth was determined by palpation, and animals were sacrificed when liver metastases were palpable. Procedures involving living animals were conducted under pathogen-free conditions and according to guidelines from the Animal Care Committee at the Generalitat de Catalunya. The Committee for Animal Experimentation at the Institute of Biomedical Research of Bellvitge (Barcelona) approved these studies.

PDO and culture conditions

Human colorectal tumors were obtained from Parc de Salut MAR Biobank (MARbiobank. Written informed consent was obtained from all participants and protocols were approved by Hospital del Mar' Ethics Committee (approval number 2019/8595/I), the Spanish regulations, and the Helsinki declaration's Guide. For PDOs generation, primary or xenografted human colorectal tumors were disaggregated in 1.5 mg/mL collagenase II and 20 µg/mL hyaluronidase after 40 min of incubation at 37 °C, filtered in 100 µm cell strainer, and seeded in 50 µL Matrigel in 24-well plates. After polymerization, 450 µL of complete medium was added (DMEM/F12 plus penicillin (100 U/mL) and streptomycin (100 µg/mL), 100 µg/mL Primocin, 1× N2 and B27, 10mM Nicotinamide; 1.25mM N-Acetyl-L-cysteine, 100

ng/mL Noggin and 100 ng/mL R-spondin-1, 10 µM Y-27632, 10nM PGE2, 3µM SB202190, 0.5µMA8301, 50 ng/mL EGF and 10nM Gastrin I). In the different experiments, PDOs were collected and digested with an adequate amount of trypsin to single cells and replated in culture. Cultures were maintained at 37 °C, 5% CO2 and medium changed every week. PDOs were expanded by serial passaging and kept frozen in liquid Nitrogen for being used in subsequent experiments.

Wound-healing assay

A pipette was used to scratch the cell-monolayer. The cells were then washed with medium. Images were obtained at various time points with aZeiss Vert.A1 micrsocope. and the migration distance was analyzed using Image J.

In vitro PDOs adhesion and migration assay

PDOs were grown in 3D for 15 days in complete medium and were collected and transferred to adherent 24-well plates with Dulbecco's modified Eagle's medium plus 10% fetal bovine serum. Migration was measured by the increase in the area of the PDOs from the starting point (0 h) until the end point (24 or 48 h depending on the PDO) of the experiment. Area was quantified using ImageJ software. Images were obtained with aZeiss Vert.A1 microscope.

In vitro Transwell assay

This assay was performed using chambers containing polycarbonate filters (8 µm pore size, Costar). CRC cells ($1X10^5$) in DMEM + 0,1% FBS were added to the upper chamber. The lower chamber was filled with DMEM + 10% FBS after 4h incubation at 37ºC. After 24 h to 72 h incubation, cells were fixed with methanol at -20ºC for 10 min and stained with 0.5% crystal violet in 25% methanol at room temperature for 15 min. The chambers were washed with PBS several times to remove excess dye. The cells on the underside were counted.

In vitro clonogenic assay

300 single CRC cells were plated in 96well plates in 10 µL Matrigel. After 11 days in culture, the number of 3D structures in each well was counted, photographs were taken with an Olympus BX61 microscope at the indicated time points for diameter determination using Adobe Photoshop. Cell viability was measured using the CellTiter-Glo 3D Cell Viability Assay following manufacturer's instructions in an Orion II multiplate luminometer.

Lentiviral transduction of CRC cells

lentiCRISPR v2 plasmid was used for knock-out experiments and TRC1.5 pLKO.1-puro was used for knock-down experiments. The sgRNA against CHUK gene were designed using Benchling and are available at supplementary Table S7. Lentiviral production was performed by transfecting HEK293T cells the lentiviral vectors and the plasmid of interest. One day after transfection, the medium was changed,

and viral particles were collected 24 h later and then concentrated using Lenti-X Concentrator. PDOs were infected by resuspending single cells in concentrated virus diluted in complete medium, centrifuged for 1 h at 650 rcf, and incubated for 5h at 37 °C. Cells were then washed in a complete culture medium and seeded as described above. Cell lines were infected by incubating cells in concentrated virus diluted in medium overnight, medium was then refreshed.

Immunohistochemical staining

Paraffin blocks were obtained from tissues, PDOs and cell lines, the previous fixation in 4% formaldehyde overnight at room temperature. Paraffin-embedded sections of 4 µm, for tissues, and 2.5 µm, for PDOs and cell lines, were deparaffinized, rehydrated and endogenous peroxidase activity was quenched (20 min, 1.5% H2O2). Citrate-based antigen retrieval was used. All primary antibodies were diluted in PBS containing 1% BSA, incubated overnight at 4 °C, and developed with the Envision+ System HRP Labeled Polymer anti-Rabbit or anti-Mouse and 3,3'-diaminobenzidine (DAB) or EnVision FLEX HRP Magenta Substrate Chromogen System (Dako) in the case of double IHC, for the appropriate time. In order to achieve optimal visualization of the protein, an amplification cascade reaction may be required using Polyclonal Goat Anti-Rabbit Immunoglobulins/Biotinylated (Dako) and Streptavidin-Peroxidase Polymer Ultrasensitive (Merck). Samples were mounted in DPX or Aquatex and images were obtained with an Olympus BX61 microscope.

The IHC analysis of tumor samples was performed by two pathologists with expertise in tumors of the digestive tract (MI and ML-L) in an independent review process.

Immunofluorescence analysis

For tissues and PDOs, the same protocol as IHC was followed. However, the samples were developed with Tyramide Signal Amplification System (TSA) and mounted in DAPI Fluoromount-G. For cell lines, cells were fixed with Paraformaldehide 4% and following permeabilization and blockage was performed with 4% milk and 0.3% Triton X-100 in PBS. All primary antibodies were diluted blocking solution, incubated overnight at 4 °C. Secondary antibodies were diluted with 4% milk in PBS and mounted in DAPI Fluoromount-G. Images were taken in an SP5 upright confocal microscope (Leica).

Hematoxylin and eosin staining

Previously de-paraffinized sections were incubated with hematoxylin 30s, tap water 5min, 80% ethanol 0.15% HCl 30s, water 30 s, 30% ammonia water (NH3(aq)) 30s, water 30s, 96% ethanol 5min, eosin 3s, and absolute ethanol 1 min. Samples were dehydrated, and mounted in DPX, and images were obtained with an Olympus BX61 microscope.

Cell lysis and Western Blot

PDOs and cell lines were lysed for 20 min on ice in 200µL of PBS plus 0.5% Triton X-100, 1mM EDTA, 100mM NA-orthovanadate, 0.2mM phenyl-methylsulfonyl fluoride, and complete protease and

phosphatase inhibitor cocktails. Lysates were analyzed by Western Blot using standard SDS–polyacrylamide gel electrophoresis (SDS-PAGE) techniques. In brief, protein samples were boiled in Laemmli buffer, run in polyacrylamide gels, and transferred onto polyvinylidene difluoride (PVDF) membranes. The membranes were incubated with the appropriate primary antibodies overnight at 4 °C, washed, and incubated with specific secondary horseradish peroxidase–linked antibodies. Peroxidase activity was visualized using the enhanced chemiluminescence reagent and autoradiography films.

RT-qPCR analysis

Total RNA from cell lines and PDOs was extracted with the RNeasy Mini Kit and RNeasy Micro Kit respectively, and cDNA was produced with the RT-First Strand cDNA Synthesis Kit. RT-qPCR was performed in LightCycler 480 system using SYBR Green I Master Kit. Samples were normalized relative to the housekeeping genes TBP and/or GAPDH. Primers used for RT-qPCR are listed in Supplementary Table S7.

Bulk RNA-seq data analysis

Libraries for both primary tumor and metastasis were simultaneously prepared and sequenced using Illumina HiSeq2500 platform (50bp paired-end reads). Samples sequencing depth ranged between 24M and 41M reads (average 31M reads) per sample.

Colorectal Tumoroid (primary tumor) samples. Quality control was performed on raw data with FASTQC tool (v0.11.9). Raw reads were trimmed to remove adapters presence with Trimgalore (v0.6.6) [59]. Default parameters were used except for a minimum quality of 15 (Phred score) and an adapter removal stringency of 3bp overlap. Trimmed reads were aligned to reference genome with STAR aligner tool (v2.7.8). STAR was executed with default parameters except for the number of allowed mismatches which was set to 1. Required genome index was built with corresponding hg38 gtf and fasta files retrieved from Ensembl (http://ftp.ensembl.org/pub/release-106/). Obtained BAM files with uniquely mapped reads were considered for further analysis. Raw gene expression was quantified using featureCounts tool from subRead software (v2.0.1) with exon as feature [60]. Obtained raw counts matrix was imported into R Statistical Software environment (v4.3.1) for downstream analysis. Raw expression matrix included 61,552 genes per 4 samples in total. Experimental design considered two existing conditions: 2xIKKα WT and 2xIKKα KO. Prior to statistical analysis, those genes with less than 5 raw counts across the 4 samples under test were removed. After pre-filtering, 20,826 genes were available for testing. For visualization purposes, counts were normalized by variance-stabilizing transformation method as implemented in DESeq2 R package [61] (v1.40.2). Differential expression analysis (DEA) was conducted with DESeq2. Fitted statistical model included sample condition as covariable with WT as the reference. Primary tumor samples were separately tested from metastasis samples since the latter showed larger within-group variability than the primary ones. Obtained log2 fold change values were shrunken with apeglm shrinkage estimator R package (v1.22.1) [62] . Raw p-values were adjusted for multiple testing using the Benjamini-Hochberg False Discovery Rate (FDR) (Benjamini & Hochberg,

1995). Differentially Expressed Genes (DEGs) between KO and WT samples were called with adjusted p-values (FDR) < 0.05 and shrunken |log2 Fold change| > 1.

Hepatic Metastases derived from PDO samples. Same general methodology as in previous paragraph was applied for the hepatic metastasis derived samples except for the reference genome. Since these samples where derived from PDO, an in-silico combine human-mouse reference genome was used instead as described by other authors [63]. Specifically, hg38 and mm39, both retrieved from Ensembl (release 106) were combined. After alignment, only those reads mapping to human assembly were considered for further analysis. Raw expression matrix included 61,552 genes per 6 samples in total (3xIKKα met-WT and 3xIKKα met- KO). This matrix was combined with raw counts from primary tumor samples for conducting differential expression analysis. Since both types of samples were simultaneously processed, no technical batch effect was expected. Experimental design considered one variable with four levels from the combination of samples origin and condition, specifically, 2xIKKα prim-WT, 2xIKKα KO, 3xIKKα met-WT and 3xIKKα met-KO. Prior to statistical analysis, those genes with less than 5 raw counts across the 10 samples under test were removed. After pre-filtering, 23,036 genes were available for testing. Following contrasts were explored: met-KO vs prim-KO, met-WT vs prim-WT and met-KO vs prim-WT.

Gene Set Enrichment analysis (GSEA). Pre-ranked Gene Set Enrichment Analysis (GSEA) was conducted over the ranked list of genes based on the shrunken log2FC obtained from differential expression analysis. GSEA was conducted through fgseaMultilevel function from fgsea R package (v1.24.0) with default parameters. GSEA interrogated the obtained cluster signatures derived from PDO single cell RNAseq data. Enrichment plots were generated with the same package.

Single cell RNA-seq data analysis

Data pre-processing. 10x sequencing raw reads were demultiplexed and aligned with 10x Genomics CellRanger v7.2.0 (cellranger count) under default parameters which includes intronic reads [64]. Sequences were aligned against the mouse pre-built reference transcriptome *refdata-gex-GRCh38-2020-A* provided by 10x Genomics. Features, barcodes and expression matrices were separately obtained per sample: 1xIKKα WT, 1xIKKα KO and 1xIKKα KO + inhibited CLDN2. Respectively for WT, KO and KO+inh CLDN2 conditions, (i) the recovered cells were 7,746, 5,367 and 6,751 cells, (ii) the median genes per cell was 6,160, 6,756 and 6,353 genes and, (iii) the mean reads per cell was 51,439, 77,820 and 60,624 reads.

Quality Control. Generated filtered matrices from CellRanger were imported and merged into R (v4.3.1) using Seurat package (v5.0.0) [65]. Seurat object with a total of 36,601 genes and 19,864 cells was obtained. Doublets were separately detected by sample with scDblFinder package (v1.14.0) [66]. For this purpose, random and cluster-based approaches, implemented in the same package, were used. Additionally, the latter was considered with the clusters identified by CellRanger software (graph-based). Those cells detected as doublets by two out of the three cases were finally labelled as doublets and

removed from the dataset. Next, cells were filtered based on the number of genes removing those with less than 500 or more than 10k genes. Cells with more than 15% of mitochondrial gene content or with less than 3500 counts were also discarded. Genes not present in at least 10 cells were filtered out. Ribosomal genes were as well discarded. After quality control, a Seurat object with a total of 25,642 genes and 14,074 cells was used for downstream analysis.

Samples Integration and Clustering. Samples were normalized using the SCTransform function regressing the mitochondrial content out and with the method glmGamPoi (package v1.12.2). After normalization, samples were integrated with the anchor-based CCA integration method implemented in Seurat. The integrated dataset was used for downstream analysis. For dimensionality reduction and visualization, runPCA and runUMAP functions were executed considering 37 principal components which corresponded to a cumulative captured data variance > 85%. Cell phase score was computed with CellCycleScoring function and available S and G2M genes in Seurat package. Clustering analysis was performed with FindNeighbors (37 dimensions) and FindClusters (resolution 0.3) obtaining a total of 10 clusters. Cluster representative genes were obtained from SCT assay with FindConservedMarkers function (adjusted p-value < 0.05, |logFC| > 0.5, cell percentage cluster of interest > 0.25). To select the top 50 representative per cluster, marker genes were sorted in descendent order by the minimum logFC among the three conditions. Normalized expression values were imputed and smoothed with MAGIC algorithm through Rmagic package (v2.0.3.999)[67].

EpiHR and Tight Junction signatures scoring. Score values were computed for 'Tight Junction Organization' (GO:0120193) GO BP term and the High-Relapse (EpiHR) signature of Cañellas-Socias et al. For this purpose, UCell R package was used (v2.4.0) [68] based on expression values from MAGIC. Additionally, per signature, cells were classified as 'Low' or 'High' based on their obtained UCell scores (High > Q3, Low for the rest of cases). Cutoff was independently obtained per condition.

Proteomics analysis

Tissue lysis/Trypsin Digestion. Cell pellets were resuspended in 100ul of ice cold 8M urea/50Mm Tris HCL with phosphatase and protease inhibitors (Roche). Each sample was sonicated (Syclon Ultrasonic Homogenizer) for 2 x 9 seconds at a power setting of 25% to disrupt the cell pellet. The protein samples were normalized to 300ug. Each sample was reduced by adding 8mM dithiothreitol (dtt) and mixing (thermomixer 1000rpm, 30°C) for 30 min and carboxylated by adding 20 mM iodoacetamide and mixing (thermomixer 1000rpm, 30°C) for 30 min the dark. The solution was diluted with 50mM Tris HCL to bring the urea concentration down to below 2M. NB: (Urea must be below 2M to prevent inhibition of trypsin). The samples were digested overnight with trypsin (1:50 enzyme to protein ratio) with gentle shaking (thermomixer 850rpm, 37°C). The digestion was terminated by adding triflouroacetic acid to 1% final concentration and cleaned up using c18 (Sep-Pak C18, Vac Cartridges). Peptides were eluted in 100µl of 60% acetonitrile 0.1% trifluoroacetic acid. Prior to phosphopeptide enrichment, 10µl was removed for proteomic analysis, vacuum centifuged and resuspended in 0.1% trifluoroacetic acid. The remanining 90ul was kept for phosphopeptide.

Phosphopeptide Enrichment. Phosphopeptide enrichment was carried out with TiO2 (Titansphere Phos-TiO Bulk 10 um, (GL Sciences Inc, Tokyo, Japan) using an adapted method previously described [69]. In summary, each sample was incubated with TiO2 beads for 30 minutes by rotation in 80% acetonitrile, 6% trifluoroacetic acid, 5mM monopotassium phosphate, 20mg/ml 2,5- dihydroxybenzoic acid, this step was carried out twice. The beads were washed 4 times in 80% acetonitrile/1% trifluoroacetic acid, before elution of the phosphopeptides with 50% acetonitrile, 7% ammonium hydroxide. The two eluents from each sample were then pooled and dried down.

LCMSMS Method (Bruker timsTof Pro/Evosep One).Samples were run on a Bruker timsTof Pro mass spectrometer connected to an Evosep One liquid chromatography system. Tryptic peptides were resuspended in 0.1% formic acid and each sample was loaded on to an Evosep tip. The Evosep tips were placed in position on the Evosep One, in a 96-tip box. The autosampler is configured to pick up each tip, elute and separate the peptides using a set chromatography method (30 samples a day)[70]. The mass spectrometer was operated in positive ion mode with a capillary voltage of 1450 V, dry gas flow of 3 l/min and a dry temperature of 180 °C. All data was acquired with the instrument operating in trapped ion mobility spectrometry (TIMS) mode. Trapped ions were selected for ms/ms using parallel accumulation serial fragmentation (PASEF). A scan range of (100-1700 m/z) was performed at a rate of 5 PASEF MS/MS frames to 1 MS scan with a cycle time of 1.03s [71].

Data Analysis (proteomics/phospho-proteomics).The raw data was searched against the Homo sapien subset of the Uniprot Swissprot database (reviewed) using the Fragpipe proteomics pipeline (version 22) with specific parameters for trapped ion mobility spectra data dependent acquisition (TIMS DDA). In the case of proteomics analysis, the LFQ-MBR workflow was selected. Detail includes MS Fraggers parameters: percursor mass tolerance +/-20ppm, fragment mass tolerance +/-20ppm, strict trypsin, variable modifications oxidation of methionine and N-terminal acetylation. Phospho-proteomic analysis was processed using the LFQ-phospho workflow which includes phosphorylation as a variable modification on serine, threonine and tyrosine residues**.** Differentially expressed proteins were identified using LFQ values. Average LFQ for each group was used to calculate the ration between PDO IKKα knockout cells and PDO IKKα WT cells. TTEST was used to determine statistical significance. Cut off of 2-fold changes in expression and p value of <0.05 were used to identify proteins that are statistically significant (Supplementary Table S3).

Cancer Colorectal (CRC) patients metacohort

An in-house metacohort of 1,118 CRC patients was generated by integrating publicly available datasets stored in Gene Expression Omnibus repository (GEO), specifically: GSE14333, GSE143985, GSE17536, GSE17537, GSE33114, GSE38832 and GSE39582. All selected datasets were generated with HG-U133_Plus_2 Array microarray Affymetrix platform. Normalization was performed by dataset using fRMA R package (v1.54.0)[72]. Batch effect was removed by using dataset as covariate using ComBat function from sva R package (v3.50.0)[73]. The final CRC metacohort is stored, as an RData object, at Zenodo (doi: 10.5281/zenodo.13303050). This object contains one data frame referring to the patients' phenotypic

information, including disease free survival (DFS) time and event and other data frame referring to the normalized and batch corrected microarray expression data.

Survival analysis over CRC patients metacohort

Survival analysis was assessed using Kaplan-Meier curve estimates considering the in-house CRC patients metacohort. For this purpose, only those patients in Stage II or III were considered. Patients were classified into two subgroups, 'High' or 'Low', based on the mean expression of specific signature genes i.e. cluster marker genes obtained from scRNA-seq data. Cutoff point was set to Q3. In case a gene is targeted by more than one array probe, the probe showing the highest expression is selected. Right-censoring was applied for saturating survival curves up to 60 months. A Log-rank test was applied to assess statistical significance between both subgroups. A p-value<0.05 was considered statistically significant. All the survival analyses and graphs were performed with the survival (v.3.5-5)[74] and survminer (v0.4.9) R packages.

Mouse scRNA-seq data exploration from Cañellas-Socias et al. 2022

The AKTP MTOs scRNA-seq dataset from Cañellas-Socias et al. [36] was downloaded from Synapse (https://www.synapse.org/#!Synapse:syn35000645). An already pre-processed. RData file was retrieved referring to all stages. This included merged data from four Smart-Seq2 experiments, each corresponding to: primary tumor, micro-, small- and macro-metastases. Data was imported into R Statistical Software (v.4.3.1) by means of Seurat R package (v5.0.0) [65]. MAGIC SCT assay (non-integrated data) was used for visualization purpose. Specifically, the expression levels from genes annotated to 'Tight Junction Organization' (GO:0120193) GO BP[75] term was explored. Heatmap was generated with ComplexHeatmap R package (v2.16.0)[76].

Quantification and Statistical analysis

Each experiment shown in the manuscript has been repeated at least twice. Statistical parameters, including number of events quantified, standard deviation and statistical significance, are reported in the figures and in the figure legends. GraphPad Prism 9 software was used for statistical analysis and p-value<0.05 is considered significant (****p-value<0.0001, ***p- value<0.001, **p-value<0-01 and n.s. *p*-value > 0.05). Statistical significance among groups was determined by Student's t-test (data fitting normal distribution) or Mann Whitney U test (data not fitting normal distribution) for two-group comparison or one-way ANOVA with Tukey's correction for multiple comparison testing.

Abbreviations

Patient-derived organoid (PDO), Colorectal cancer (CRC), Epithelial-to-mesenchymal transition (EMT), Tight junction proteins (TJP), American Type Culture Collection (ATCC), 3,3'-diaminobenzidine (DAB)

Declarations

Ethics Approval

This work was approved by the ethics Committee at Hospital del Mar on March 10th 2023 with number 2022/10639/I,

Consent for publication

All authors have read and approved the final manuscript and consent its publication

Data availability

Single-cell and bulk RNA-seq datasets generated in this study have been deposited in NCBI Gene Expression Omnibus (GEO) repository under GEO SuperSeries accession no. GSE274368, composed in three SubSeries GSE274321 (10x scRNAseq data), GSE274325 (bulk RNA-seq Primary Tumor) and GSE274326 (bulk RNA-seq Hepatic Metastasis derived from PDO.

The following secure token has been created to allow review of record GSE274368 while it remains in private status: qnydgyugbfotbmd

Proteomics data are available via ProteomeXchange with identifier PXD057102.

Reviewers can access the dataset by logging in to the PRIDE website using the following account details:

Username: reviewer_pxd057102@ebi.ac.uk and Password: B34C5cn4Yp0kç

Code availability

Scripts that have been used to process the in house scRNA-seq and bulk RNA-seq datasets are deposited in Github repository:

https://github.com/BigaSpinosaLab/PAPER_Tight_Junctions_CRC_liver_metastasis

Competing Interests

The authors declare no competing interests related with this work.

Funding

This work was funded by grants from Instituto de Salud Carlos III FEDER (PI22/00069) cofunded by the EU, Generalitat de Catalunya 2021SGR39 and Instituto de Salud Carlos III-Fondo Europeo de Desarrollo Regional (CIBERONC; CB16/12/00244). We thank MarBiobank for providing and characterizing patient samples (PT20/00023 from Instituto de Salud Carlos III FEDER) and to SFI Comprehensive Molecular Analytical Platform (CMAP) for proteomic analysis (grant 18/RI5702). D.A-V. is a recipient of the FI20/00130 grant from Instituto de Salud Carlos III FEDER. T.L-J. is a recipient of the AECC postdoctoral grant POSTD21975. L.S. is a postdoctoral researcher supported by AGAUR (Programa Investigo 2022

2022; INV-1 00005 /100005ID5). M.M. is a recipient of a grant from the Instituto Carlos III, grant number CA22/00011 (cofunded by the European Social Fund Plus, ESF+, co-financed by the European Union). AV is funded by Instituto de Salud Carlos III FEDER (PI22/00548). KW is funded by SFI Comprehensive Molecular Analytical Platform (CMAP), reference 18/RI5702.

Authors Contributions

DA-V, JB, JA-M and DH prepared the reagents and performed the majority of the experiments with cells; MM, EC and TL-J performed the statistical analyses of data; VG-H and PH-M performed flow cytometry analysis, DM, KW and IB performed the proteomic analysis of PDOs; AV, DA-V and MM-I performed the *in vivo* experiments of metastasis; ML-L, AT and EA performed histopathologic evaluation of tumor samples; LE, MI and AB conceptualized and conducted the study, analyzed data and prepared the manuscript.

Acknowledgments

We want to thank Espinosa's and Bigas' lab members for constructive discussions and suggestions.

Reporting summary

Further information on research design is available in the Nature Research Reporting Summary linked to this article.

References

1. Biller, L. H. & Schrag, D. Diagnosis and Treatment of Metastatic Colorectal Cancer: A Review. *JAMA* **325**, 669–685 (2021).
2. Thiery, J. P., Acloque, H., Huang, R. Y. J. & Nieto, M. A. Epithelial-mesenchymal transitions in development and disease. *Cell* **139**, 871–90 (2009).
3. Mani, S. A. *et al.* The Epithelial-Mesenchymal Transition Generates Cells with Properties of Stem Cells. *Cell* (2008) doi:10.1016/j.cell.2008.03.027.
4. Yang, J. *et al.* Guidelines and definitions for research on epithelial-mesenchymal transition. *Nat. Rev. Mol. Cell Biol.* **21**, 341–352 (2020).
5. Perl, A. K., Wilgenbus, P., Dahl, U., Semb, H. & Christofori, G. A causal role for E-cadherin in the transition from adenoma to carcinoma. *Nature* **392**, 190–3 (1998).
6. Cano, A. *et al.* The transcription factor Snail controls epithelial–mesenchymal transitions by repressing E-cadherin expression. *Nat. Cell Biol.* **2**, 76–83 (2000).
7. Batlle, E. *et al.* The transcription factor Snail is a repressor of E-cadherin gene expression in epithelial tumour cells. *Nat. Cell Biol.* **2**, 84–89 (2000).
8. Aggarwal, V., Montoya, C. A., Donnenberg, V. S. & Sant, S. Interplay between tumor microenvironment and partial EMT as the driver of tumor progression. *iScience* **24**, 102113 (2021).

9. Pastushenko, I. *et al.* Fat1 deletion promotes hybrid EMT state, tumour stemness and metastasis. *Nature* **589**, 448–455 (2021).
10. Kröger, C. *et al.* Acquisition of a hybrid E/M state is essential for tumorigenicity of basal breast cancer cells. *Proc. Natl. Acad. Sci. U. S. A.* **116**, 7353–7362 (2019).
11. Donato, C. *et al.* Hypoxia Triggers the Intravasation of Clustered Circulating Tumor Cells. *Cell Rep.* **32**, 108105 (2020).
12. Friedl, P. & Mayor, R. Tuning Collective Cell Migration by Cell-Cell Junction Regulation. *Cold Spring Harb. Perspect. Biol.* **9**, (2017).
13. Campbell, N. R. *et al.* Cooperation between melanoma cell states promotes metastasis through heterotypic cluster formation. *Dev. Cell* **56**, 2808-2825.e10 (2021).
14. Gkountela, S. *et al.* Circulating Tumor Cell Clustering Shapes DNA Methylation to Enable Metastasis Seeding. *Cell* **176**, 98-112.e14 (2019).
15. Friedl, P. & Gilmour, D. Collective cell migration in morphogenesis, regeneration and cancer. *Nat. Rev. Mol. Cell Biol.* **10**, 445–457 (2009).
16. Aceto, N. *et al.* Circulating tumor cell clusters are oligoclonal precursors of breast cancer metastasis. *Cell* **158**, 1110–1122 (2014).
17. Chen, Q. *et al.* A narrative review of circulating tumor cells clusters: A key morphology of cancer cells in circulation promote hematogenous metastasis. *Front. Oncol.* **12**, 944487 (2022).
18. Fanning, A. S., Jameson, B. J., Jesaitis, L. A. & Anderson, J. M. The tight junction protein ZO-1 establishes a link between the transmembrane protein occludin and the actin cytoskeleton. *J. Biol. Chem.* **273**, 29745–53 (1998).
19. DiDonato, J. A., Mercurio, F. & Karin, M. NF-κB and the link between inflammation and cancer. *Immunol. Rev.* **246**, 379–400 (2012).
20. Staudt, L. M. Oncogenic activation of NF-kappaB. *Cold Spring Harb. Perspect. Biol.* **2**, a000109 (2010).
21. Xia, Y., Shen, S. & Verma, I. M. NF-κB, an active player in human cancers. *Cancer Immunol. Res.* **2**, 823–30 (2014).
22. Stilmann, M. *et al.* A Nuclear Poly(ADP-Ribose)-Dependent Signalosome Confers DNA Damage-Induced IκB Kinase Activation. *Mol. Cell* **36**, 365–378 (2009).
23. Huang, T. T., Wuerzberger-Davis, S. M., Wu, Z.-H. & Miyamoto, S. Sequential Modification of NEMO/IKKγ by SUMO-1 and Ubiquitin Mediates NF-κB Activation by Genotoxic Stress. *Cell* **115**, 565–576 (2003).
24. Wu, Z.-H. *et al.* ATM- and NEMO-Dependent ELKS Ubiquitination Coordinates TAK1-Mediated IKK Activation in Response to Genotoxic Stress. *Mol. Cell* **40**, 75–86 (2010).
25. Margalef, P. *et al.* BRAF-induced tumorigenesis is IKKα-dependent but NF-κB–independent. *Sci. Signal.* **8**, ra38–ra38 (2015).

26. Colomer, C. *et al.* IKKα Kinase Regulates the DNA Damage Response and Drives Chemo-resistance in Cancer. *Mol. Cell* **75**, 669-682.e5 (2019).
27. Pecharromán, I. *et al.* IκB kinase-α coordinates BRD4 and JAK/STAT signaling to subvert DNA damage-based anticancer therapy. *EMBO J.* e114719 (2023) doi:10.15252/embj.2023114719.
28. Luo, J. L. *et al.* Nuclear cytokine-activated IKKα controls prostate cancer metastasis by repressing Maspin. *Nature* (2007) doi:10.1038/nature05656.
29. Toll, A. *et al.* Active nuclear IKK correlates with metastatic risk in cutaneous squamous cell carcinoma. *Arch. Dermatol. Res.* **307**, 721–729 (2015).
30. Zou, Z. *et al.* Maspin, a serpin with tumor-suppressing activity in human mammary epithelial cells. *Science* **263**, 526–9 (1994).
31. Zhang, J. *et al.* Identification of CD44 as a downstream target of noncanonical NF-κB pathway activated by Human T-cell leukemia virus type 1-encoded Tax protein. *Virology* **413**, 244–252 (2011).
32. Smith, S. M., Lyu, Y. L. & Cai, L. NF-κB Affects Proliferation and Invasiveness of Breast Cancer Cells by Regulating CD44 Expression. *PLoS One* **9**, e106966 (2014).
33. Alonso-Marañón, J. *et al.* Combination of chemotherapy with BRAF inhibitors results in effective eradication of malignant melanoma by preventing ATM-dependent DNA repair. *Oncogene* **40**, 5042–5048 (2021).
34. Colomer, C., Pecharroman, I., Bigas, A. & Espinosa, L. Targeting IKKα kinase to prevent tumor progression and therapy resistance. *Cancer Drug Resist.* (2020) doi:10.20517/cdr.2019.104.
35. Dukes, J. D., Whitley, P. & Chalmers, A. D. The PIKfyve inhibitor YM201636 blocks the continuous recycling of the tight junction proteins claudin-1 and claudin-2 in MDCK cells. *PLoS One* **7**, e28659 (2012).
36. Cañellas-Socias, A. *et al.* Metastatic recurrence in colorectal cancer arises from residual EMP1+ cells. *Nature* **611**, 603–613 (2022).
37. van Laarhoven, H. W. M. & Derks, S. Claudin-18.2 targeting by zolbetuximab: results of SPOTLIGHT in perspective. *Lancet (London, England)* **401**, 1630–1631 (2023).
38. Nakayama, I. *et al.* Claudin 18.2 as a novel therapeutic target. *Nat. Rev. Clin. Oncol.* **21**, 354–369 (2024).
39. Hu, M. C. T. *et al.* IκB Kinase Promotes Tumorigenesis through Inhibition of Forkhead FOXO3a. *Cell* **117**, 225–237 (2004).
40. Vreka, M. *et al.* IκB Kinase α Is Required for Development and Progression of KRAS -Mutant Lung Adenocarcinoma. *Cancer Res.* **78**, 2939–2951 (2018).
41. Karin, M. & Greten, F. R. NF-κB: linking inflammation and immunity to cancer development and progression. *Nat. Rev. Immunol.* **5**, 749–759 (2005).
42. Xie, W. *et al.* IKBKE phosphorylates and stabilizes Snail to promote breast cancer invasion and metastasis. *Cell Death Differ.* **29**, 1528–1540 (2022).

43. Lee, D.-F. & Hung, M.-C. Advances in targeting IKK and IKK-related kinases for cancer therapy. *Clin. Cancer Res.* **14**, 5656–62 (2008).
44. Mauro, C., Zazzeroni, F., Papa, S., Bubici, C. & Franzoso, G. The NF-κB Transcription Factor Pathway as a Therapeutic Target in Cancer: Methods for Detection of NF-κB Activity. in *Methods in molecular biology (Clifton, N.J.)* vol. 512 169–207 (2009).
45. Awasthee, N. *et al.* Targeting IκappaB kinases for cancer therapy. *Semin. Cancer Biol.* **56**, 12–24 (2019).
46. Ping, H., Yang, F., Wang, M., Niu, Y. & Xing, N. IKK inhibitor suppresses epithelial-mesenchymal transition and induces cell death in prostate cancer. *Oncol. Rep.* **36**, 1658–64 (2016).
47. Ghosh, D., Dutta, A., Kashyap, A., Upmanyu, N. & Datta, S. PLP2 drives collective cell migration via ZO-1-mediated cytoskeletal remodeling at the leading edge in human colorectal cancer cells. *J. Cell Sci.* **134**, (2021).
48. DeCamp, S. J. *et al.* Epithelial layer unjamming shifts energy metabolism toward glycolysis. *Sci. Rep.* **10**, 18302 (2020).
49. Labuschagne, C. F., Cheung, E. C., Blagih, J., Domart, M.-C. & Vousden, K. H. Cell Clustering Promotes a Metabolic Switch that Supports Metastatic Colonization. *Cell Metab.* **30**, 720-734.e5 (2019).
50. Lu, W. & Kang, Y. Epithelial-Mesenchymal Plasticity in Cancer Progression and Metastasis. *Dev. Cell* **49**, 361–374 (2019).
51. Pastushenko, I. & Blanpain, C. EMT Transition States during Tumor Progression and Metastasis. *Trends Cell Biol.* **29**, 212–226 (2019).
52. Bakir, B., Chiarella, A. M., Pitarresi, J. R. & Rustgi, A. K. EMT, MET, Plasticity, and Tumor Metastasis. *Trends Cell Biol.* **30**, 764–776 (2020).
53. Lüönd, F. *et al.* Distinct contributions of partial and full EMT to breast cancer malignancy. *Dev. Cell* **56**, 3203-3221.e11 (2021).
54. Arumugam, T. *et al.* Trefoil factor 1 stimulates both pancreatic cancer and stellate cells and increases metastasis. *Pancreas* **40**, 815–22 (2011).
55. Bougen, N. M. *et al.* Trefoil factor 1 suppression of E-CADHERIN enhances prostate carcinoma cell invasiveness and metastasis. *Cancer Lett.* **332**, 19–29 (2013).
56. Spadazzi, C. *et al.* Trefoil factor-1 upregulation in estrogen-receptor positive breast cancer correlates with an increased risk of bone metastasis. *Bone* **144**, 115775 (2021).
57. Ahmed, A. R. H., Griffiths, A. B., Tilby, M. T., Westley, B. R. & May, F. E. B. TFF3 is a normal breast epithelial protein and is associated with differentiated phenotype in early breast cancer but predisposes to invasion and metastasis in advanced disease. *Am. J. Pathol.* **180**, 904–916 (2012).
58. Cui, H.-Y. *et al.* CD147 receptor is essential for TFF3-mediated signaling regulating colorectal cancer progression. *Signal Transduct. Target. Ther.* **6**, 268 (2021).

59. Krueger, F., James, F., Ewels, P., Afyounian, E. & Schuster-Boeckler, B. FelixKrueger/TrimGalore - DOI via Zenodo. (2020) doi:https://zenodo.org/record/7598955#.ZGOKAi8RpR4.
60. Liao, Y., Smyth, G. K. & Shi, W. featureCounts: an efficient general purpose program for assigning sequence reads to genomic features. *Bioinformatics* **30**, 923–930 (2014).
61. Love, M. I., Huber, W. & Anders, S. Moderated estimation of fold change and dispersion for RNA-seq data with DESeq2. *Genome Biol.* **15**, 550 (2014).
62. Zhu, A., Ibrahim, J. G. & Love, M. I. Heavy-tailed prior distributions for sequence count data: removing the noise and preserving large differences. *Bioinformatics* **35**, 2084–2092 (2019).
63. Callari, M. *et al.* Computational approach to discriminate human and mouse sequences in patient-derived tumour xenografts. *BMC Genomics* **19**, 19 (2018).
64. Zheng, G. X. Y. *et al.* Massively parallel digital transcriptional profiling of single cells. *Nat. Commun.* **8**, 14049 (2017).
65. Hao, Y. *et al.* Dictionary learning for integrative, multimodal and scalable single-cell analysis. *Nat. Biotechnol.* **42**, 293–304 (2024).
66. Germain, P.-L., Lun, A., Garcia Meixide, C., Macnair, W. & Robinson, M. D. Doublet identification in single-cell sequencing data using scDblFinder. *F1000Research* **10**, 979 (2021).
67. van Dijk, D. *et al.* Recovering Gene Interactions from Single-Cell Data Using Data Diffusion. *Cell* **174**, 716-729.e27 (2018).
68. Andreatta, M. & Carmona, S. J. UCell: Robust and scalable single-cell gene signature scoring. *Comput. Struct. Biotechnol. J.* **19**, 3796–3798 (2021).
69. Kelstrup, C. D. *et al.* Performance Evaluation of the Q Exactive HF-X for Shotgun Proteomics. *J. Proteome Res.* **17**, 727–738 (2018).
70. Bache, N. *et al.* A Novel LC System Embeds Analytes in Pre-formed Gradients for Rapid, Ultra-robust Proteomics. *Mol. Cell. Proteomics* **17**, 2284–2296 (2018).
71. Meier, F. *et al.* Online Parallel Accumulation-Serial Fragmentation (PASEF) with a Novel Trapped Ion Mobility Mass Spectrometer. *Mol. Cell. Proteomics* **17**, 2534–2545 (2018).
72. McCall, M. N., Bolstad, B. M. & Irizarry, R. A. Frozen robust multiarray analysis (fRMA). *Biostatistics* **11**, 242–53 (2010).
73. JT, L. *et al.* sva: Surrogate Variable Analysis. (2025).
74. A, T. T. Package for Survival Analysis in R. (2024).
75. Ashburner, M. *et al.* Gene ontology: tool for the unification of biology. The Gene Ontology Consortium. *Nat. Genet.* **25**, 25–9 (2000).
76. Gu, Z., Eils, R. & Schlesner, M. Complex heatmaps reveal patterns and correlations in multidimensional genomic data. *Bioinformatics***32**, 2847–9 (2016).

Figures

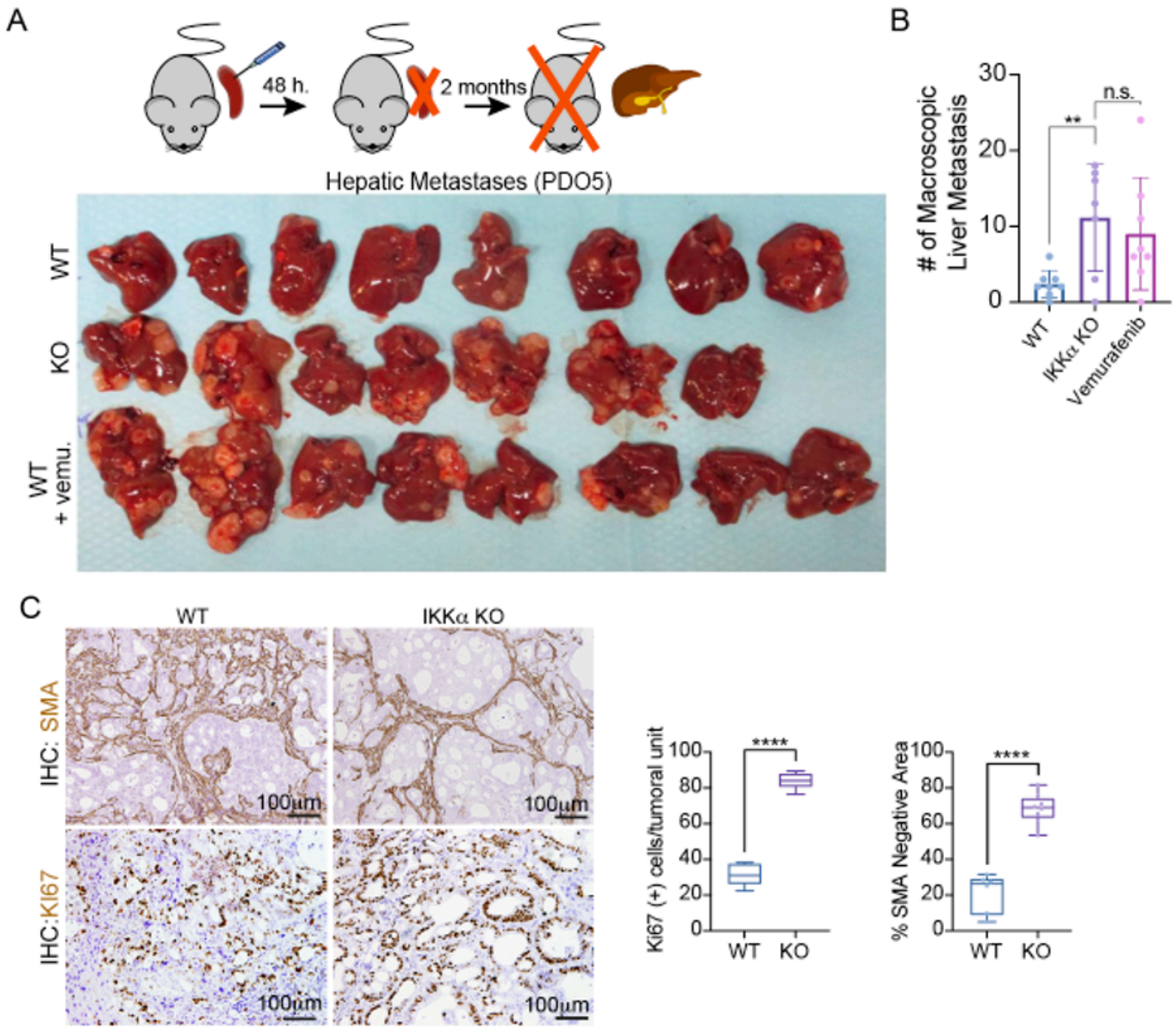

Figure 1

Genetic depletion of IKKα increases the metastatic potential of patient-derived organoid cells.

(A, B) Schematic representation of the strategy used for the vivo intrasplenic metastasis assay with PDO5 in nude mice and photograph of the liver metastases developed. One of the three experiments performed is shown (A). Bar chart with the quantification of the number of macroscopic metastases in the different experimental conditions WT, IKKa KO and WT followed by vemurafenib treatment, from the experiment in A (B).

(C) Representative microscopic images of the immunohistochemistry analysis of the activated fibroblast marker SMA and the proliferation marker KI67 in the livers of mice transplanted with PDO5 of the indicated genotypes. Quantification of the data.

Statistical tests; (B) Ordinary one-way ANOVA and Tukey's multiple comparisons test (**p-value<0.01 and n.s. *p*-value > 0.05); (C) Statistical test: Unpaired t test (**p*-value < 0.05 and n.s. *p*-value > 0.05).

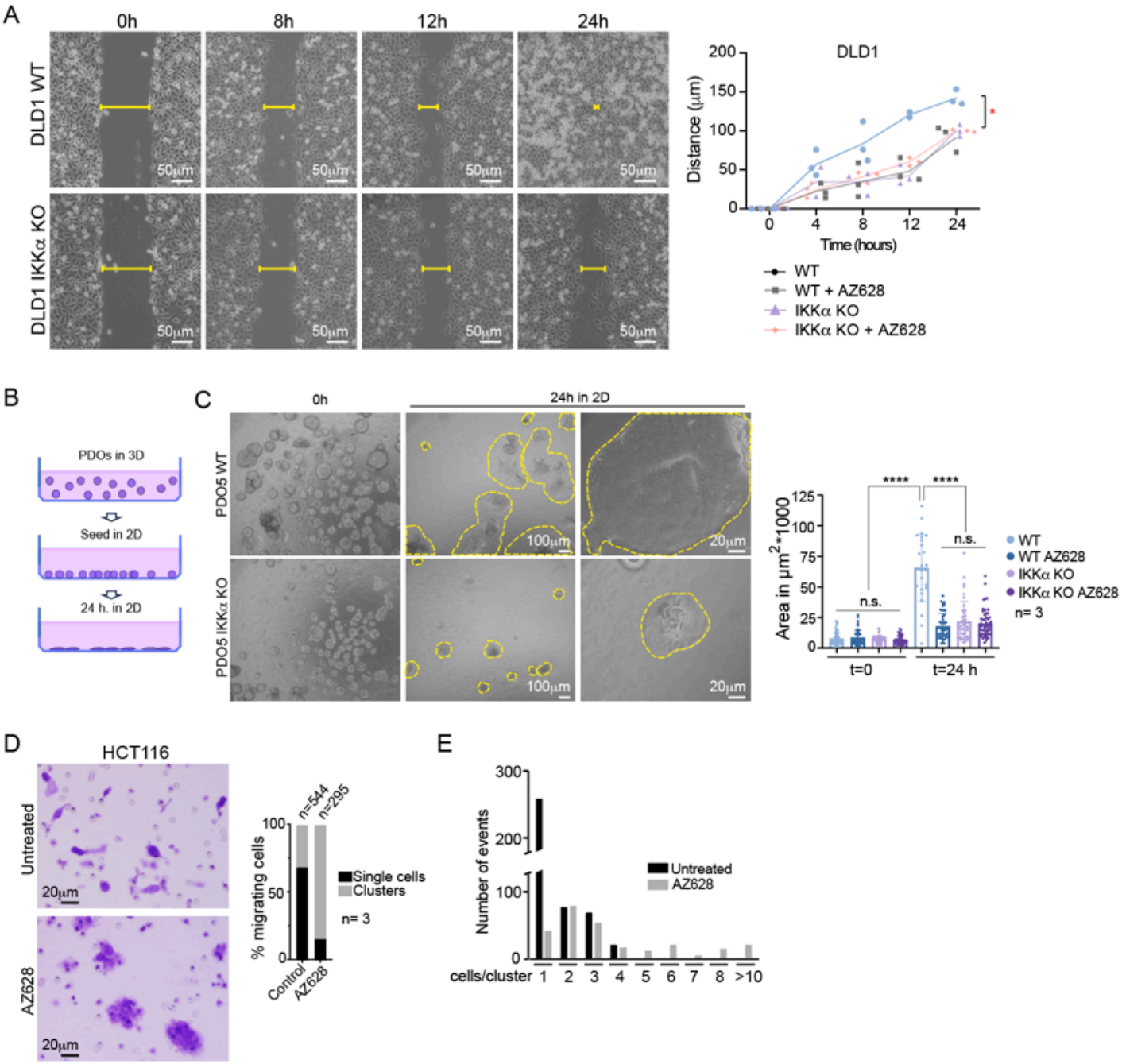

Figure 2

Functional depletion of IKKα alters the migratory behavior of cancer cells.

(A) Representative images of wound-healing assay of DLD1 WT and IKKα KO cells. Dot plot shows the quantification of wound closure at each time point (n=3) per condition. Line connects mean values per time point.

(B, C) Schematic representation of the experiments in which PDOs were adapted to grow in adherent (2D) conditions (B). Representative images of WT and IKKα KO PDO5 cells seeded in adherent 2D conditions and quantification of the area covered by the colonies at the indicated time points and experimental conditions (WT and IKKα KO untreated or treated with AZ628 at 10 μM) (C). Bars indicate mean values, and error bars refer to ± standard deviation.

(D, E) Representative images of untreated or AZ628-treated (8 μM) HCT116 cells in the transwell inserts at 24h, and quantification of the number of single cells or cell clusters in the filter (D). Quantification of the number of cells per cluster in each condition (E).

Statistical tests; (A) two-way ANOVA and Šídák's multiple comparisons test at 24h (***p-value<0.001, **p*-value < 0.05 and n.s. *p*-value > 0.05). (C) Ordinary one-way ANOVA and Tukey's multiple comparisons test (****p-value < 0.0001, n.s. p-value > 0.05).

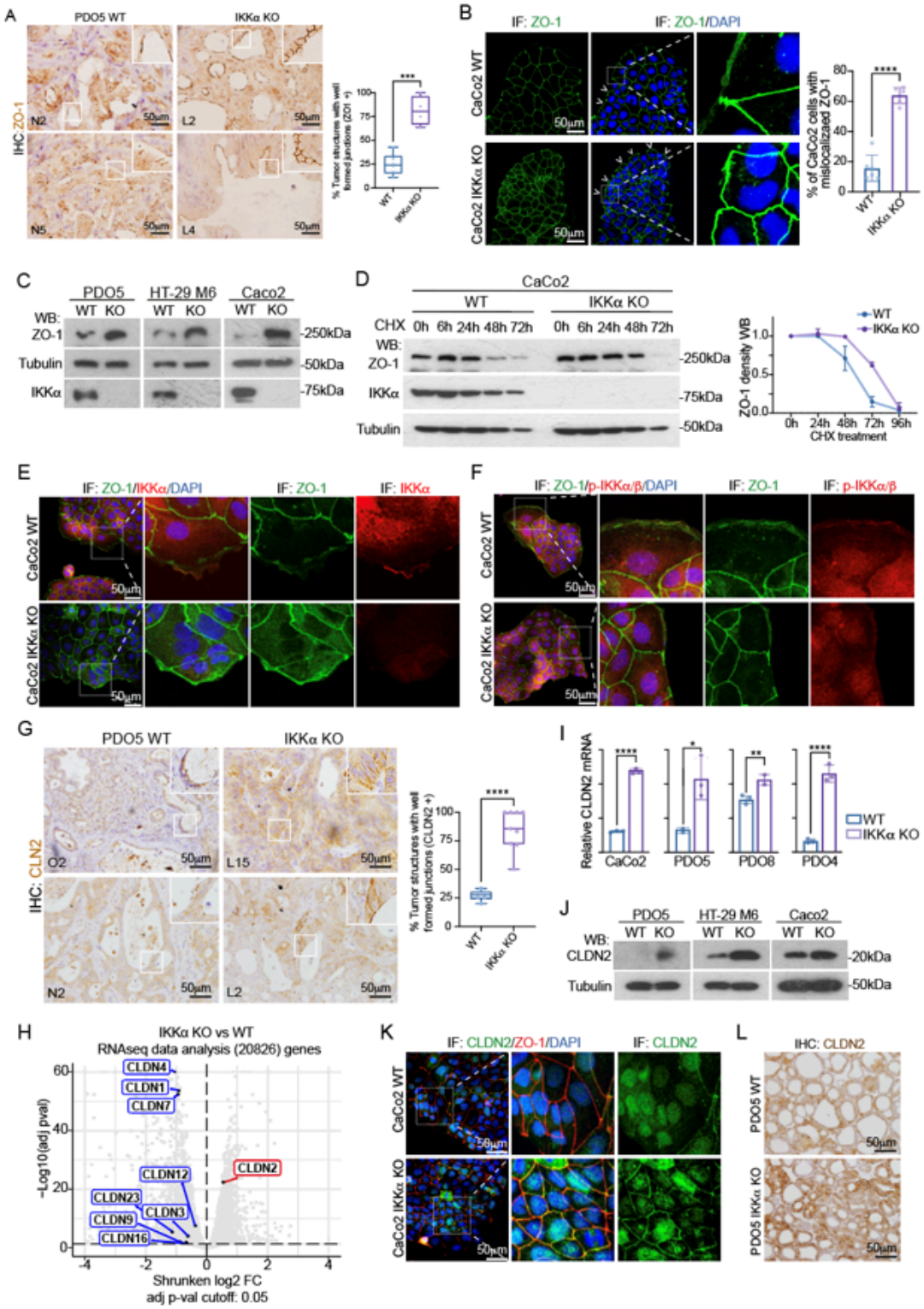

Figure 3

IKKα regulates ZO-1 protein stability and cellular distribution.

(A) Microscopic images of the immunohistochemistry analysis of ZO-1 in WT and IKKα KO-derived metastases. Boxplot with the quantification of the tumor structures with well-formed cell-cell contacts

positive for ZO-1 in the metastases derived from WT and IKKα KO PDO5 cells. Boxplot shows the median (center line) first and third quartiles (box limits) and whiskers extend to minimum and maximum values.

(B) Representative images of immunofluorescence staining of ZO-1 in WT and IKKα KO CaCo2 cells and quantification of cells displaying the indicated patterns of staining.

(C, D) WB analysis of ZO-1 levels in the indicated WT and IKKα KO cell lines (C), or CaCo2 cells WT and IKKα KO treated with cycloheximide (0,025 µg/µL) and collected at the indicated time points (D). Densitometric quantification of the ZO-1 band from 3 independent experiments performed.

(E, F) Representative images of double immunofluorescence analysis of IKKα (E) or active p-IKKα/b (F) and ZO-1 in WT and IKKα KO CaCo2 cells.

(G) Microscopic images of the immunohistochemistry analysis of CLDN2 in WT and IKKα KO-derived metastases. Boxplot with the quantification of the tumor structures with well-formed cell-cell contacts positive for CLDN2 in the metastases derived from WT and IKKα KO PDO5 cells.

(H) Volcano plot from bulk RNA-seq differential expression analysis comparing IKKα KO against WT PDO5 cells. Detected members of Claudins protein family are highlighted.

(I, J) RT-qPCR (I) and WBanalysis (J) of CLDN2 in the indicated WT and IKKα KO cell lines. Bars in panel I indicate mean values, and error bars refer to ± standard deviation.

(K) Representative images of a double immunofluorescence staining of CLDN2 and ZO-1 in WT and IKKα KO CaCo2 cells.

(L) Representative images of CLDN2 immunohistochemistry in WT and IKKα KO PDOs.

Statistical tests; (A, B, G and I) unpaired two-tailed t-test (****p-value<0.0001, ***p-value<0.001, **p-value<0-01, *p-value < 0.05 and ns p-value > 0.05).

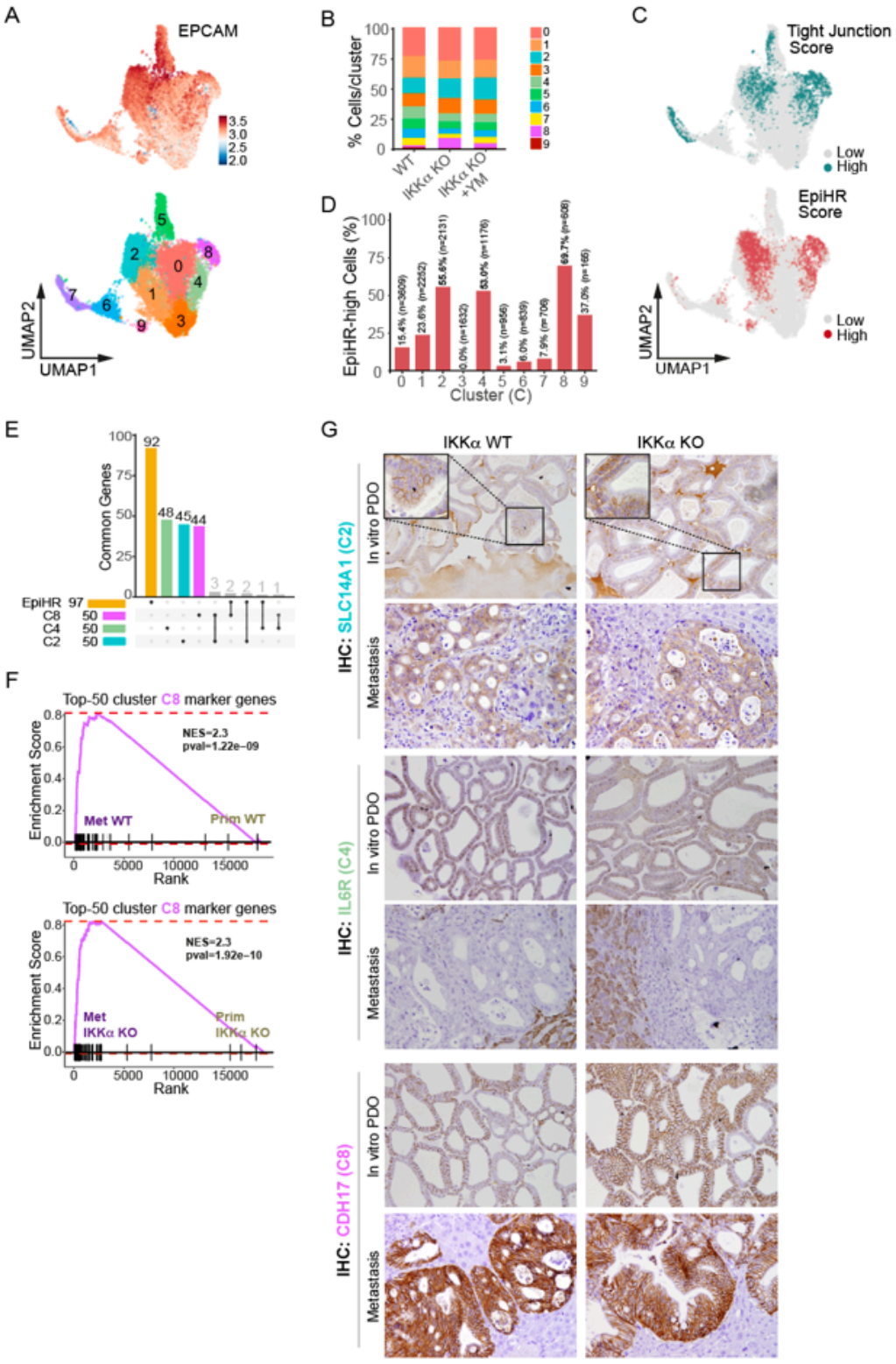

Figure 4

Cell clusters characterized by tight junction and high-relapse signatures are enriched in the liver metastases.

(A) UMAP representations (top) of integrated scRNA-seq data from PDO5 cells in three experimental conditions (WT, IKKα KO, and IKKα KO treated with CLDN2 inhibitor for 16h) showing the expression

levels of the epithelial marker EPCAM (upper panel) and the 10 identified clusters (lower panel).

(B) Stacked bar plot showing the percentage of cells annotated to each cluster per experimental condition.

(C) UMAP showing the cell classification into high or low score levels of the 'Tight Junction Organization' term from Gene Ontology database (GO:0120193) (upper panel) and the High-Relapse (EpiHR) signature, which identify early metastatic populations (Cañellas-Socias et al., 2022) (lower panel).

(D) Bar graph showing the percentage of cells labeled as high EpiHR score per identified cluster. The number of cells per cluster is shown. Note that clusters C2, C4 and C8 have percentages greater than 50%.

(E) Upset plot showing common and exclusive number of genes among the top-50 marker genes obtained from clusters C2, C4 and C8 and EpiHR signature genes. Importantly, marker genes of these clusters are conserved among the three experimental conditions studied.

(F) GSEA results from liver metastasis and primary tumor PDO5 WT (top) and IKKa KO (bottom) cellsagainst the top-50 cluster 8 marker genes.

(G) IHC analysis of PDO5 cells in 3D cultures and the hepatic metastases derived from them using the indicated antibodies, which are characteristic of clusters C2, C4 and C8.

(UMAP: Uniform Manifold Approximation and Projection)

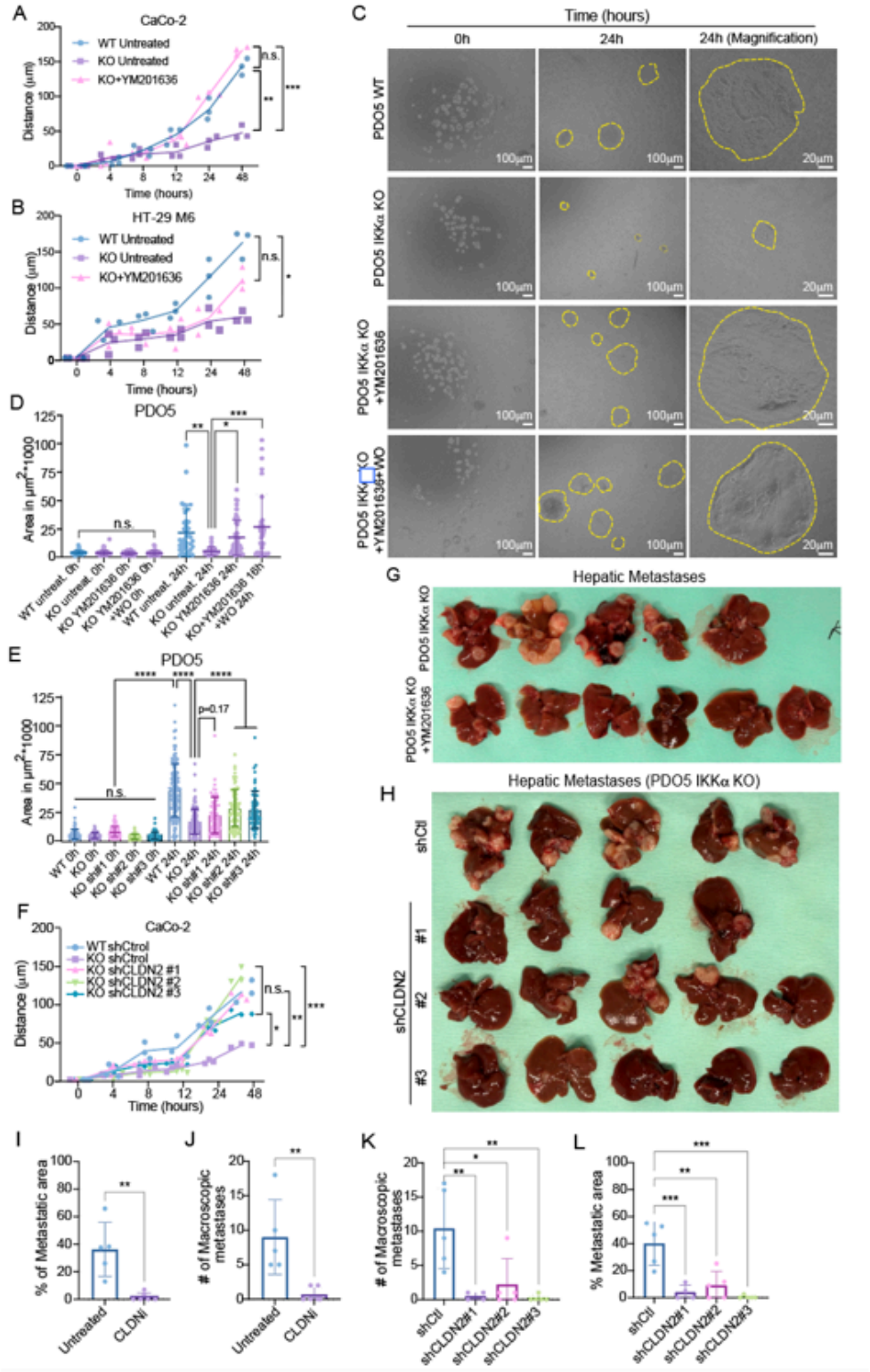

Figure 5

Targeting CLDN2 activity reverts the migratory mode imposed by IKKα deficiency and suppresses the metastatic potential of CRC cells *in vivo*.

(A, B) Quantification of wound-healing migration assay of CaCo2 (A) and HT-29 M6 (B) cells WT, IKKα KO and IKKα KO treated with the CLDN2 inhibitor YM201636 (0.5 µM).

(C, D) Representative images of the 2D adaptation assay in WT, IKKαKO and IKKα KO PDO5 cells treated with YM201636 (C) and quantification of the area covered by the colonies at the indicated time points and conditions (D).

(E) Quantification of the area covered in the 2D adaptation assay by the colonies of PDO5 WT, IKKα KO and IKKα KO transduced with the indicated shCLDN2 constructs.

(F) Quantification of the migration in the wound-healing assay of CaCo2 IKKα KO cells transduced with shCtrol or shCLDN2 #1, #2, #3).

(G) Photograph of the hepatic metastases developed in nude mice upon intrasplenic injection of PDOs IKKα KO or IKKα KO pre-treated with YM201636 (0.5 µM) for 16h previous to the implantation in the mouse.

(H) Photograph of the hepatic metastases developed in nude mice upon intrasplenic injection of PDOs IKKα KO shCtrol or shCLDN2 #1, #2 or #3.

(I, J, K, L) Quantification of the experiments shown in G (I, J) and H (K, L).

Statistical test (A, B and F): two-way ANOVA and Tukey's multiple comparisons test. (D, E, K and L) Ordinary one-way ANOVA and Tukey's multiple comparisons test. (I and J) unpaired t test (****p-value<0.0001, ***p-value<0.001, **p-value<0-01, *p-value < 0.05 and ns p-value > 0.05).

Supplementary Files

This is a list of supplementary files associated with this preprint. Click to download.

- TableS1BulkRNAseqDEAPrimaryandMetastasis.xlsx
- TableS2scRNAseqCRCTumoroidIKKaClusterMarkers.xlsx
- TableS3Proteomics.xlsx
- TableS4GSEAClustersMETPRIM.xlsx
- SupplementaryFigLegendsFinal.docx